Quantitative laser diagnostics on trimethylindium pyrolysis and photolysis for functional nanoparticle growth

OPEN ACCESS
IOP Publishing
Measurement Science and Technology
Meas. Sci. Technol. **33** (2022) 055201 (10pp)
https://doi.org/10.1088/1361-6501/ac51a4

Quantitative laser diagnostics on trimethylindium pyrolysis and photolysis for functional nanoparticle growth

Per Samuelsson[1,*], Martin H Magnusson[2], Knut Deppert[2], Marcus Aldén[1] and Zhongshan Li[1]

[1] Division of Combustion Physics, Lund University, Box 118, SE-221 00 Lund, Sweden
[2] Division of Solid State Physics and NanoLund, Lund University, Box 118, SE-221 00 Lund, Sweden

E-mail: per.samuelsson@forbrf.lth.se

Received 30 November 2021, revised 31 January 2022
Accepted for publication 3 February 2022
Published 17 February 2022

Abstract

We report on an optical investigation of the pyrolysis and photolysis of trimethylindium (TMIn) as a typical metalorganic precursor for functional nanowire growth, aiming at an in-depth understanding of the governing chemistry and optimization of aerosol-based (aerotaxy) and epitaxial growth processes. A flow reactor with special consideration given to optical access was built to provide the chemical environment for *in situ* optical measurements on the pyrolysis and photolysis of TMIn. By probing a resonant transition of the indium atom, high-resolution laser absorption and laser-induced fluorescence spectroscopy were applied to obtain the atomic indium concentration at different chosen conditions in a spatially and temporally resolved manner. The results indicate that quantitative measurements of indium atoms under growth conditions are feasible. A 213 nm pulsed laser was employed to induce photolytic dissociation of TMIn vapor under chosen conditions. The photolytic dissociation of TMIn vapor with an ultraviolet laser turns out to be a promising method in generating substantial chemical effects, indicated by the generation of visible clouds of indium particles, and high concentrations of indium atoms far beyond the pyrolytically generated amount.

Supplementary material for this article is available online

Keywords: pyrolysis, photolysis, laser-induced fluorescence, aerosols, metalorganic vapor phase epitaxy, trimethylindium, indium

(Some figures may appear in color only in the online journal)

* Author to whom any correspondence should be addressed.

1. Introduction

Metalorganic vapor-phase epitaxy (MOVPE) is the most common technique for industrial scale production of semiconductors for use in light-emitting diodes. Until now, existing gas-phase laser diagnostic studies in MOVPE environments have dealt mainly with surface growth, through probing the chemical environment above the growth substrate using line-of-sight methods or point measurement techniques, including absorption spectroscopy [1, 2], spontaneous Raman spectroscopy [3–5], and coherent anti-Stokes Raman spectroscopy [6]. Due to the strong influence of surfaces on reaction rates, one aspect complicating kinetic modeling of MOVPE processes is the influence of the reactor geometry, resulting in locally different environmental conditions. Here, spatially resolved planar laser-induced fluorescence (PLIF) provides a unique possibility to map the concentration of gas phase species, as well as temperature with high sensitivity. Moreover, with recent activity oriented towards gas-phase growth of semiconductors, there is currently a dearth of on-line diagnostic tools for probing the distributed growth environment with respect to key parameters including temperature and gas-phase species concentrations. In aerotaxy, nanometer-sized catalytic seed particles are mixed with the precursors in the gas phase, and the growth environment is distributed in all three dimensions [7, 8], but modeling efforts are impeded by the lack of *in situ* diagnostic information. Furthermore, growth occurs continuously without any interfering substrate, making it an ideal environment for *in situ* optical diagnostics. By monitoring the chemical gas phase environment simultaneously with the growing nanowires, the growth process can in principle be optimally controlled. The aim of the present study is to extend the array of optical diagnostic tools to on-line, quantitative, operando imaging of key parameters inside the reactor environment to support comprehensive kinetic modeling of MOVPE and aerotaxy processes. Our approach is based on high-resolution laser spectroscopy on gas-phase species, and the feasibility of the approach is demonstrated by measurement of indium atoms that exist both naturally under MOVPE and aerotaxy growth conditions from thermal decomposition of trimethylindium (TMIn), and artificially generated by pulsed laser photolysis of TMIn.

Growth of III–V semiconductor nanowires is possible within a narrow temperature window, governed by thermodynamics. Below 770 K, growth is limited by reaction kinetics and incorporation of carbon atoms [9], whereas above 870 K, it is limited by parasitic reactions on reactor walls and homogeneous reactions in the gas phase. TMIn decomposes pyrolytically as [10, 11]:

$$\mathrm{In(CH_3)_3} \rightarrow \mathrm{In(CH_3)_2} + \mathrm{CH_3}, \tag{1}$$

$$\mathrm{In(CH_3)_2} \rightarrow \mathrm{InCH_3} + \mathrm{CH_3}, \tag{2}$$

$$\mathrm{InCH_3} \rightarrow \mathrm{In} + \mathrm{CH_3}, \tag{3}$$

$$\ldots$$

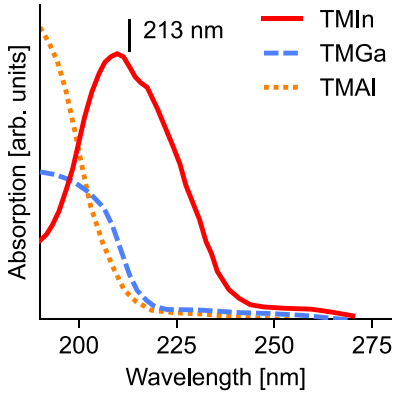

Figure 1. Overview of the absorption spectra of three group III metalorganic precursors, adapted from Beuermann and Stuke [12]. The fifth harmonic of the neodymium-doped yttrium aluminum garnet (Nd:YAG) fundamental emission wavelength, used in this study for pulsed photodissociation of TMIn, is indicated at 213 nm.

where reaction (3) was reported to occur above 750 K [4], i.e. above 750 K, free indium atoms can be expected in the reactor environment.

In order to investigate this in a controlled environment, a model reactor was constructed, being able to heat the reactants to the temperature required by the growth conditions, with special consideration given to optical access. Due to the high reactivity of metalorganic precursors, contamination of water and oxygen to the environment must be avoided. This is achieved by only allowing inert materials in contact with the heated flow, and by shielding the optical probe region with inert gas. The reactor is described in detail in the next section.

Another major goal of this work is to explore the possibilities of optically manipulating, controlling, and ideally enhancing the growth process. Using a focused laser beam to locally stimulate growth could provide a way to study the growth process without influence of surfaces, either thermally by heating the seed particles to enhance the local supersaturation, or chemically by photolytically decomposing the gas phase precursors. As will be discussed, surfaces introduce a hysteretic effect which presents difficulties with systematic studies.

Shown in figure 1 are the absorption spectra of three common group III precursors—TMIn, trimethylgallium (TMGa), and trimethylaluminum (TMAl)—which are characterized by broad absorption bands in the deep ultraviolet (UV). The absorption spectrum of TMIn peaks near 210 nm [2, 12], and absorption of a deep UV photon in this region results in excitation to a dissociative excited state [12]. The following dissociation mechanism was proposed [12]:

$$\mathrm{In(CH_3)_3} + h\nu \rightarrow \mathrm{In\,(CH_3)_2^*} + \mathrm{CH_3}, \tag{4}$$

$$\mathrm{In\,(CH_3)_2^*} \rightarrow \mathrm{In} + \mathrm{C_2H_6}, \tag{5}$$

i.e. upon absorption of an UV photon with energy $h\nu$, TMIn decomposes into a methyl fragment and excited dimethylindium, which rapidly decomposes into an indium atom and ethane.

The photolysis and pyrolysis processes of TMIn were studied using a pump–probe technique comprising pulsed photodissociation of TMIn and continuous wave (CW) detection of the photofragments. A ns-pulsed UV laser was employed to photodissociate TMIn, producing high concentrations of atomic indium. The photolytically produced indium atoms were then detected using a separate probe laser, using a combination of high-resolution atomic absorption spectroscopy, PLIF, and elastic scattering (ES). Detection of both absorption and PLIF under the same conditions enables visualization of the atomic indium distribution and concentration during pyrolysis and photolysis.

The experimental investigation is divided into two parts: quantitative measurements of indium atoms during pyrolysis (section 2), and during UV laser photolysis of TMIn (section 3).

2. TMIn pyrolysis

2.1. Pyrolysis reactor

Vapor-phase TMIn was delivered to the reactor using a metalorganic vapor delivery system, schematically depicted on the left-hand side in figure 2. The solid TMIn sample (adduct grade, SAFC Hitech) was contained in a commercial bubbler. TMIn vapor was carried to the reactor by flowing nitrogen (99.9999% N_2) through the bubbler, which was maintained at ambient pressure and 283 K using a circulation bath (PolyScience). The carrier gas was additionally filtered through a gas purifier (MicroTorr, SAES) upstream of the bubbler, to remove possible contamination of oxygen and water vapor. The TMIn vapor concentration was controlled by the vapor pressure (determined by the temperature of the bubbler), the carrier gas flow rate through the bubbler (0.5 l min^{-1} typical), and a dilution flow (0.5 l min^{-1} nitrogen) after the bubbler. The gas flows were controlled using mass flow controllers (Bronkhorst). A vacuum pump was employed for purging the gas system to remove possible contamination of oxygen and water vapor. During operation, the nitrogen carrier was directed through the bubbler, carrying TMIn vapor to an electrically heated flow reactor, shown on the right-hand side in figure 2. A typical TMIn concentration of 300 ppm, neglecting any losses, was used during all experiments. The reactor was designed for full optical access horizontally to the heated TMIn vapor flow in open air, which was protected by a sheath flow of nitrogen. A cylindrical alumina (Al_2O_3) heating element (13 mm inner diameter, 18 mm outer diameter, 480 W, Rauschert, Germany) electrically heated the core reactant N_2 + TMIn flow (1.0 l min^{-1} typical), while an outer nitrogen sheath flow (25 l min^{-1} typical) prevented oxidation of TMIn by ambient air. The resistive heating element was embedded inside the heater tube wall, and only chemically inert Al_2O_3 surfaces were in contact with the reactant flow at high temperature. A stainless-steel porous frit served to laminarize the sheath flow, and a steel cylinder above the heater acted as a flow stabilizer. The volume above the frit can be filled with ceramic beads to further stabilize the sheath flow. The described system provides the possibility to study pyrolysis of TMIn at different

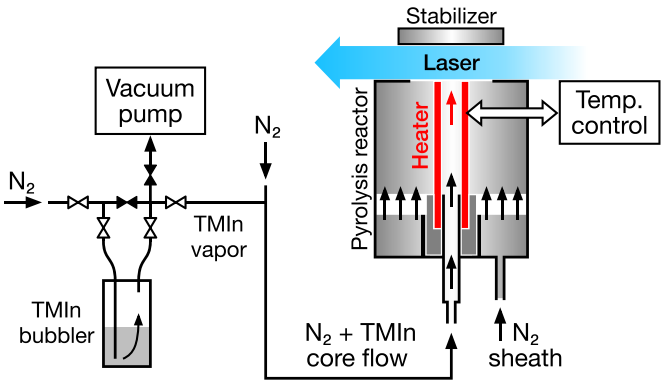

Figure 2. Cross sectional sketch of the experimental setup showing the metalorganic vapor delivery system and reactor, as seen from the side. The optical probe region is located between the heater and a flow stabilizer. Arrows indicate gas flow; ⋈ indicates open valves; ⧓ indicates closed valves.

temperatures, through *in situ* spatially and temporally resolved measurement of indium atoms.

The vapor pressure p of TMIn is given by [13]:

$$\log\left(p/\mathrm{Pa}\right) = 8.86 - 3204/\left(T/\mathrm{K}\right), \tag{6}$$

where T is the temperature of the bubbler. In order to characterize the thermodynamic conditions in the optical probe region, we measured the gas temperature 10 mm above the heater (T_{gas}) using a type K thermocouple, as a function of the temperature of the heater surface, 20 mm from the top (T_{wall}), using another thermocouple embedded in the heater wall. From a linear fit, shown in figure S1 (available online at stacks.iop.org/MST/33/055201/mmedia) in the supplementary material, the gas temperature in the optical probe region is given by:

$$T_{\mathrm{gas}}/\mathrm{K} = 0.73\left(T_{\mathrm{wall}}/\mathrm{K}\right) + 44, \tag{7}$$

when T_{wall} is within the range 420 K–1170 K. The wall temperature determines the rate of heterogeneous TMIn pyrolysis, whereas the gas temperature, estimated using equation (7), determines, e.g. the rate of homogeneous nucleation in the optical probe region. To minimize systematic errors, and for consistency, all temperatures specified in the following are heater tube wall temperatures, measured at the point where the temperature is highest.

2.2. Experimental

In order to obtain the concentration of atomic indium, we measured the absorption of the 6s $^2S_{1/2} \leftarrow$ 5p $^2P^o_{1/2}$ transition of In I at 410 nm. A partial energy level diagram of the indium atom is shown in figure 3. The 410 nm light was generated by frequency doubling the fundamental output of a CW Ti:sapphire laser (SolsTiS, M Squared Lasers) in a lithium triborate (LBO) crystal mounted inside an enhancement cavity. The fundamental wavelength was continuously monitored using a wavemeter (WS6-600, High Finesse). For wavelength-resolved measurements, the laser frequency was scanned over

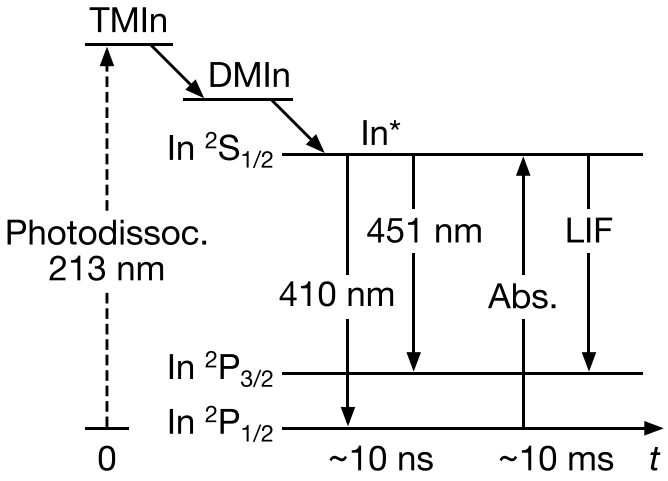

Figure 3. Adopted scheme for photodissociation of TMIn using a pulsed 213 nm laser, and CW detection of indium fragments. Shown to the right is a partial energy level diagram of the neutral indium atom. The employed detection schemes for indium are indicated by vertical arrows, where upward pointing arrows indicate absorption processes, and downward arrows indicate dissociation or spontaneous emission, e.g. laser-induced fluorescence (LIF). The $^2P_{1/2}$ ground state and the $^2S_{1/2}$ excited state of ^{115}In have two hyperfine levels each ($F = 4, 5$, not depicted). Indicated by diagonal arrows is the TMIn photodissociation pathway proposed in by Beuermann and Stuke [12].

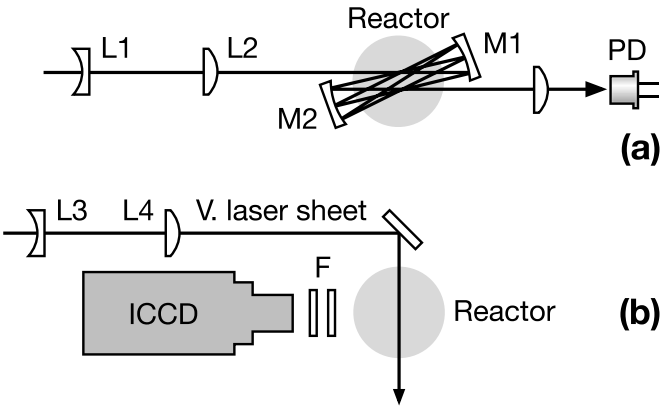

Figure 4. Top view schematic of the optical setup for high-resolution spectroscopy of atomic indium during pyrolysis, using (a) multipass absorption spectroscopy, and (b) PLIF. TMIn flows out of the figure plane. In (a), the incoming 410 nm sample beam was coupled into the multipass cavity using the lenses L1 and L2, and the absorption signal detected using a photodiode (PD). The actual number of passes was 29, and the multipass waist approximately 5 mm. All beams propagate in a horizontal plane 5 mm above the reactor. In (b), L3 and L4 (seen from the side) expands the incoming 410 nm beam vertically into a laser sheet, intersecting the TMIn vapor flow above the reactor. The resulting 451 nm fluorescence was filtered (F) and detected using an intensified charge-coupled device (ICCD) camera.

47 GHz about $\lambda_{ex} = 410.2950$ nm by applying a triangle voltage waveform to the resonator slow external input terminal on the laser controller at a rate of 0.5 Hz. The voltage waveform was generated by a data acquisition card (PCIe-6341, National Instruments), which was also used for simultaneous acquisition of the reference and sample photodiode (PD) signals.

The absorption beam path is shown in figure 4(a). Part of the 410 nm beam from the laser was picked off using a wedged glass plate, where one reflected beam acted as output power reference (not depicted). Another part (sample beam) was focused above the heater exit tube using the lenses L1 and L2 as shown in figure 4. The corresponding reference and sample signals were detected by two Si PDs (PDA36A-EC, and PDA100A2, respectively, Thorlabs). In order to increase the sensitivity of the absorption measurements, we employed a concentric multipass cavity, formed by two spherical 2″ diameter mirrors with −100 mm radius of curvature, spaced slightly less than 200 mm apart. The cavity mirrors had a specified 99.995% reflectance at 410 nm. The sample beam was matched to the cavity using L1 and L2 in figure 4(a), with focal lengths −100 and +150 mm, respectively. The cavity was centered above the reactor, and the multipass beam bundle had a waist diameter of approximately 5 mm, less than half the inner diameter of the heater tube. Using this geometry, the theoretical maximum number of passes should be slightly above 100 [14], while in practice the typical number of passes was around 30, limited by the unsteady flow and associated beam shifts due to varying refractive index gradient at higher temperatures.

In order to determine the spatial distribution of indium atoms, we employed PLIF. Atomic indium was excited from the ground state to the 6s $^2S_{1/2}$ excited state at 410 nm, and the fluorescence from 6s $^2S_{1/2}$ to 5p $^2P^o_{3/2}$ at 451 nm was detected, as shown in figure 3. Such an excitation scheme is frequently adopted for two-line atomic fluorescence (TLAF) thermometry [15]. The optical setup is shown schematically in figure 4(b). The output from the same 410 nm laser used for absorption was expanded to 6 mm diameter using a Keplerian telescope composed of two spherical lenses with focal lengths +200 and +750 mm (not depicted). The 6 mm diameter beam was further expanded vertically, and focused horizontally, using a cylindrical lens L3 with focal length −50 mm, and a spherical lens L4, with focal length +500 mm, keeping the central 19 mm of the laser sheet. The output power at 410 nm was 230 mW. The central 19 mm part of laser sheet was directed between the heater and the flow stabilizer, and horizontally focused above the heater, illustrated in blue in figure 2. The fluorescence was selected using a narrowband interference filter (450 nm center wavelength, 10 nm full width at half maximum (FWHM), Andover Corp.) and detected using an intensified charge-coupled device (ICCD) camera (PIMAX 2, Princeton Instruments) with a $f = 50$ mm, $f/3.5$ objective lens, mounted on a 21 mm extension tube. Typical integration time was 1 ms. A Schott KG5 short pass filter blocked blackbody emission from the heating element.

2.3. Results and discussion

Shown in figure 5 are laser frequency scans over part of the 410 nm In I absorption line. Also shown are fitted spectra,

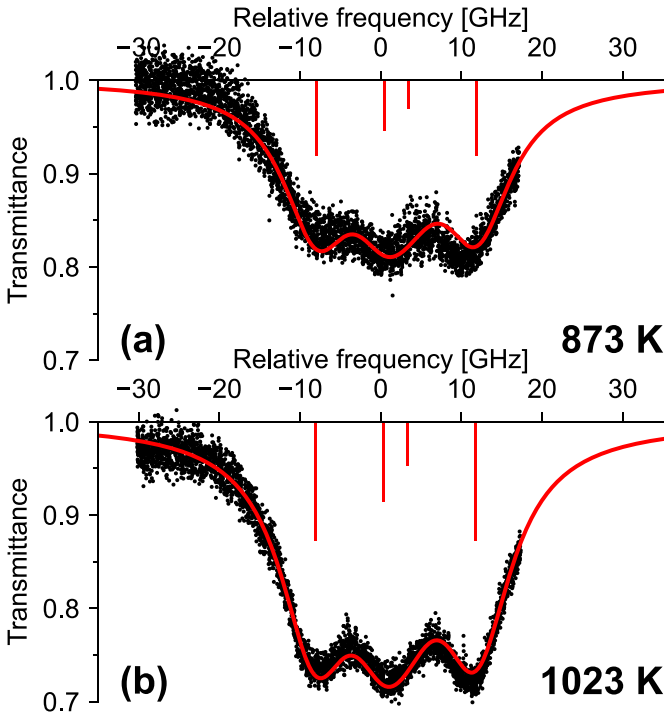

Figure 5. Multipass laser absorption scans over the 410 nm line of atomic indium at (a) 873 K and (b) 1023 K. The solid red curves are fits corresponding to atomic indium concentrations of 10 and 15 ppb, respectively. The vertical lines indicate the relative strength and frequency of each hyperfine component of the transition.

assuming Voigt line shapes and using the known frequency and relative intensity of the four hyperfine components [16]. The instrumental width of the laser is negligible. The raw spectra suffer from noise mainly from beam deflections due to unsteady gas flow; the absorption scans shown in figure 5 constitute envelopes of the collected spectra. The fitted parameters were baseline, frequency offset, Lorentzian linewidth, and the area under the fitted spectrum. The Gaussian contribution to the linewidth was fixed at the calculated Doppler width, approximately 1.3 GHz FWHM. The fitted Lorentzian contribution due to collisional broadening was 11 GHz FWHM. To account for nonuniform indium concentration along the absorption beam path, the equivalent absorption path length was estimated from figure 6(a). Assuming the indium concentration is proportional to the indium LIF intensity, the concentration of atomic indium is higher closer to the hot reactor walls, which is reflected downstream as the two 'pillars' in figure 6(a). Using a multipass absorption path length of 263 mm, the indium concentration was estimated to be 10 ppb at 873 K and 15 ppb at 1023 K.

Shown in figure 6(a) is the 451 nm LIF from indium atoms produced by thermal decomposition of TMIn inside the heater tube, at 883 K wall temperature. The intensity scale has been calibrated using the concentration obtained from the absorption scan shown in figure 5(a), assuming the LIF intensity was linear with concentration. The spatially integrated LIF signal, shown as a function of the wall temperature in figure 6(b), starts to appear at approximately 723 K. Above 723 K, the LIF signal increases exponentially with wall temperature, at

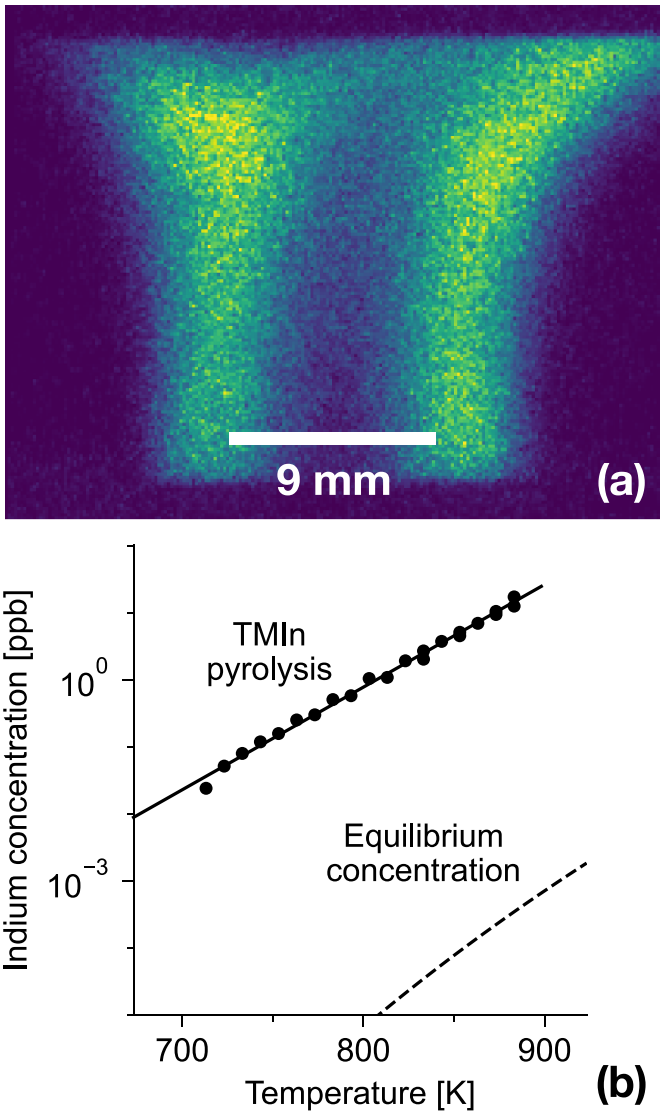

Figure 6. (a) False-color PLIF image of the indium atom distribution above the reactor during TMIn pyrolysis at 883 K. The full height of the image corresponds to the space between the reactor and flow stabilizer. The two brighter columns reflect the higher TMIn decomposition rate near the inner wall of the heater tube, below the imaged region. The scale bar indicates the equivalent single-pass absorption path length, and the vertical position of the absorption beam. Integration time was 1 ms. (b) Indium atom concentration estimated from the integrated 451 nm indium LIF, calibrated using absorption measurement at 883 K. Also shown is the expected indium concentration from vapor pressure near bulk indium metal under equilibrium conditions calculated using equation (8).

least up to 883 K, which was the maximum temperature investigated. The atomic indium concentration is bounded by the concentration of the TMIn precursor, estimated using equation (6) to be at most 300 ppm, depending on losses in the system, and of the vapor pressure p of atomic indium, given at temperatures T between 430 K and 2500 K by [17]:

$$\log\left(p/\mathrm{Pa}\right) = 10.380 - 12276/\left(T/\mathrm{K}\right), \qquad (8)$$

and shown as comparison in figure 6(b). It should be emphasized that due to the low vapor pressure of indium from bulk material, the experimental conditions do not constitute equilibrium, and that the indium concentration is governed by a differential equation where the source is the indium generated by TMIn pyrolysis, and the loss terms are condensation and diffusion, as well as flow out of the probe volume.

There is a relatively small difference between the measured concentrations at 873 K and 1023 K in figure 5, smaller than what might be expected given the exponentially increasing LIF intensity shown in figure 6(b). We attribute this inconsistency to varying TMIn vapor concentration in the system due to factors such as the solid nature of TMIn, and reactor temperature cycling and associated adsorption and desorption. The experimental data behind figures 5 and 6(b) were collected on different occasions, and the results illustrate the importance of near-simultaneous absorption and LIF measurements in systems suffering from significant adsorption of the analyte and related memory effects. If the absorption measurement and the LIF imaging were conducted simultaneously, and the TMIn concentration were allowed to reach a steady state at each temperature, which may take a significant amount of time, we would expect the results to be consistent.

Finally, it should be noted that the sensitivity of the LIF measurements is reduced by fluorescence quenching due to the N_2 ambient. Replacing either the carrier or the sheath gas with argon resulted in an increased LIF intensity but was not extensively investigated due to the associated uncertainties pertaining to gas composition when using different carrier and sheath gases, and the different fluid-dynamic and thermodynamic properties of carrier gases other than the more commonly used nitrogen.

3. Pulsed photolysis of TMIn

3.1. Experimental

In this section, we describe the optical arrangements employed for photodissociation of TMIn, and detection of the photofragments. A schematic of the experimental setup is shown in figure 7. In each experiment, atomic indium was generated by pulsed UV photodissociation of TMIn using a ns-pulsed pump laser, and the resulting atomic indium fragments were probed using a combination of spontaneous emission, LIF and absorption; particles were detected by ES. In both cases, a CW probe laser was used. The LIF and ES probe beams were vertically expanded into 19 mm tall laser sheets and directed through the gap between the reactor and the flow stabilizer, as shown in figure 2, where they were horizontally focused above the heater tube. For the absorption measurements, due to the high concentration of indium atoms generated by pulsed photolysis as compared with pyrolysis, a single pass geometry was sufficient to produce a detectable absorption signal. The absorption beam and photodissociation beams were focused approximately 5 mm above the heater and crossed at an angle of 16°.

As photolysis (pump) laser, we employed the fifth harmonic of a pulsed neodymium-doped yttrium aluminum garnet (Nd:YAG) laser emitting at 213 nm (8 ns pulse duration,

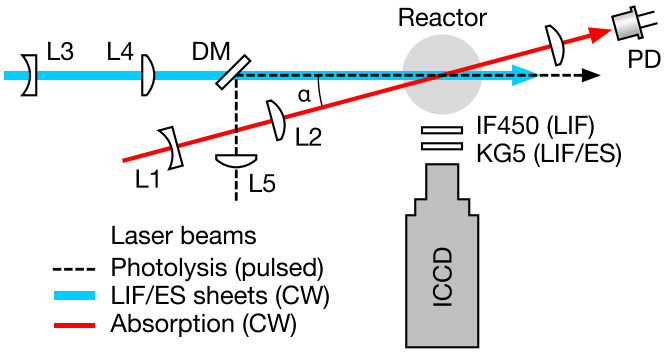

Figure 7. Overhead view of the optical setup for pump-probe spectroscopy of TMIn photolysis. The photodissociation fragments were probed using single pass absorption (red) at 410 nm, PLIF excited at 410 nm (blue) and ES at 532 nm (blue). The 213 nm photodissociation beam (black broken line) was loosely focused above the heater using lens L5. The incoming LIF/ES beams were expanded to 19 mm vertical laser sheets by lenses L3 (seen from the side) and L4 and overlapped with the photodissociation beam using a dichroic mirror (DM). The absorption beam crossed the photodissociation beam at an angle $\alpha = 16^{\circ}$, approximately 5 mm above the heater tube. PD—photodiode; IF450—450 nm bandpass filter; KG5—IR blocking filter.

10 Hz repetition rate, model Brilliant B, Quantel), which coincides with the absorption maximum of TMIn, as shown in figure 1. Typical output energy at 213 nm was 1–4 mJ per pulse. The photolysis beam, indicated by the broken line in figure 7, was focused using a spherical lens L5 to a waist diameter of 2.2 mm ($1/e^2$ energy), resulting in an energy density of 26 mJ cm^{-2} at 1 mJ.

Time-resolved absorption measurements were conducted similarly as for the multipass absorption. However, for the photolysis experiments only a single pass was used due to higher concentration of atomic indium. Furthermore, the probe laser wavelength was fixed at $\lambda_{ex} = 410.2950$ nm, and the output of the PD was recorded on an oscilloscope (TDS 340 A, Tektronix) instead of a data acquisition card. The indium absorption cross section was estimated from the line shape obtained from multipass absorption measurements and transition probabilities from National Institute of Standards and Technology (NIST) [18]. It was assumed that the absorption line shape did not change substantially during a transient.

For LIF measurements during photolysis, we used the same PLIF setup as described previously for pyrolysis, with the photodissociation beam spatially overlapped with the probe laser sheet using a dichroic mirror (DM).

Due to the much higher vapor pressure of TMIn compared to metallic indium, at sufficiently high concentration, pulsed photodissociation resulted in a supersaturated indium vapor, causing homogeneous nucleation of the photodissociation fragments, as described in the following section. The resulting indium particles generated by UV laser photodissociation were detected by their ES when illuminated with a 532 nm CW diode-pumped solid state laser (300 mW, Roithner Lasertechnik). Analogously to the LIF beam, the 532 nm beam was expanded to approximately 6 mm and collimated using two spherical lenses with focal lengths 200 and 750 mm, then

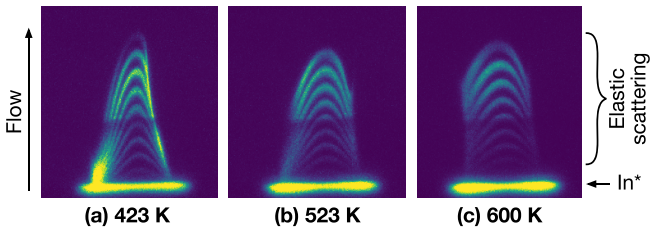

Figure 8. Multiple exposures of unfiltered ES from indium particles, at different reactor temperatures. The vertical arrow indicates the flow direction. The horizontal structure near the bottom of each image is emission from atomic indium formed in excited states (In^*) following ultraviolet photodissociation of TMIn, defining the intersection between the horizontal photodissociation beam and the vertical reactant flow. The parabolic stripes are ES from laser-generated particles, illuminated by a continuous vertical laser sheet, with the intensified CCD camera operating in multiple-exposure mode. The stripes, starting from the bottom, represents exposures at $t = 0, 5, 10, \ldots, 45$ ms after the photodissociation pulse, i.e. the stripes define timelines that visualize the reactant flow field above the reactor. The darker region in the center is due to inhomogeneities in the laser sheet.

expanded into a 19 mm vertical laser sheet using the lenses L3 and L4, as shown in figure 7.

For detection of atomic indium LIF and particle ES we used the same detection system (ICCD, objective lens and optical filters) as for the PLIF measurements during pyrolysis, shown in figure 4(b), with the exception that no bandpass filter was used for ES.

3.2. Results and discussion

Shown in figure 8 is ES from particles generated by pulsed photodissociation of TMIn and illuminated using a 532 nm CW laser sheet. The photodissociation energy was approximately 4 mJ per pulse. No flow stabilizer was used. The ICCD camera was operated in multiple-exposure mode, allowing a sequence of images of the particles to be recorded in a single frame, at different delays after a single photodissociation pulse. In each figures 8(a)–(c), the thin parabolic stripes constitute separate exposures of a single particle cloud generated by the UV photolytic laser pulse as the cloud follows the laminar carrier gas flow. The integration time was 0.5 ms at each delay, and the delay between successive exposures was 5 ms. Also shown is part of the spontaneous emission from atomic indium formed in an excited state along the photodissociation beam, which we will refer to as In^* emission in the following. The topmost stripe was recorded 45 ms after the photodissociation pulse, and its apex is located approximately 17 mm above the photodissociation beam, i.e. the flow speed in the center of the core flow can be directly read out from the images as 36 cm s^{-1}. Conceptually this is similar to molecular tagging velocimetry [19].

No attempt was made to analyze the composition of the particles generated by photodissociation. Based on the low melting point (430 K), high boiling point (2345 K) and the low vapor pressure of indium, we expect that the observed particles are liquid indium droplets, possibly mixed with hydrocarbons. Park *et al* observed particles during pyrolytic decomposition of TMIn near a heated substrate, that were believed to be condensed liquid indium droplets [4]. Creighton *et al* similarly reported observation of liquid indium nanoparticles distributed in thin layer near the substrate and determined their size using the polarization dependence of their Mie scattering [20]. Generation of Fe nanoparticles by pulsed UV laser photodissociation of metal carbonyls was discussed by Gurentsov [21].

Figure 9 depicts the indium PLIF and In^* intensity distribution under some selected conditions, specifically at different delays after the photodissociation pulse, and at two different wall temperatures. Generally, the images in each row are to be compared. Note that figure 9(c) is shown on a different intensity scale than (d). Higher temperature generally results in stronger and longer-lived indium fluorescence. After several microseconds, the LIF signal far exceeds the In^* emission intensity, and is still detectable after more than 25 ms after photodissociation at 883 K.

Some of the LIF images in figure 9 exhibit dark regions in the center of the indium plume that remains over the investigated time interval, likely caused by depletion of neutral ground state indium. The dark region is most easily seen in figure 9(c), indicated by an arrow, and would thereby develop on the timescale of 1 ms or shorter. The effect is more pronounced at lower temperature, possibly due to atomic diffusion. At 213 nm, a single photon is sufficient to ionize ground state indium. A possible explanation is therefore that neutral indium is depleted as a result of single-photon photoionization during the dissociation pulse, i.e. that one 213 nm photon dissociates TMIn into indium, which is then ionized by a second 213 nm photon. This explanation implies that the combined lifetimes of all intermediate species in the dissociation pathway are shorter than the duration of the photodissociation pulse (8 ns). Another possibility is that the dark regions are caused by depletion of free indium atoms due to supersaturation resulting in fast nucleation of indium clusters or droplets. Using shorter (ps or fs) photodissociation pulses or performing simultaneous LIF and ES measurements may help corroborating the two explanations.

Shown in figure 10 are the time-resolved results from pulsed UV photodissociation of TMIn combined with CW indium LIF, at two different temperatures, chosen to be significantly below and above the onset of reaction (3), respectively. The 213 nm photolysis pulse energy was 1 mJ. The LIF signal was isolated by subtracting the In^* emission, collected with the probe laser blocked, from images collected with both In^* emission and LIF. The signal is characterized at short delays (sub microseconds) by strong In^* emission from atomic indium formed in an excited state, and at longer delays (milliseconds) by the indium LIF signal, corresponding to the ground state population. Whereas the In^* emission decays within 1 μs at 423 K to a few μs at 883 K, the ground state population has a much longer lifetime of approximately 100 μs at 423 K, and 1 ms at 883 K before being reduced by half, as the indium atoms nucleate, or diffuse out of the probe volume. The longer lifetime at the higher temperature is compensated by a higher peak intensity of the In^* emission at the

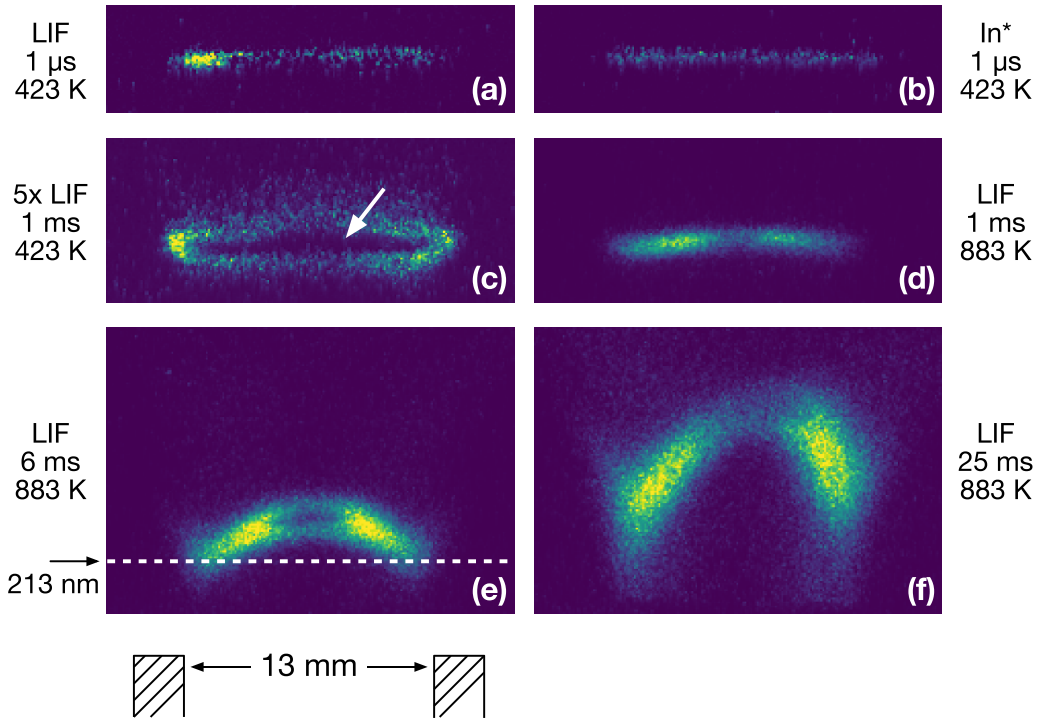

Figure 9. Indium PLIF and In* emission, collected at different temperatures, delays after the photolysis laser pulse, and using different camera gate durations. (a) LIF at 423 K, detected at 1 µs delay after the photolysis ultraviolet pulse and 200 ns gate width; (b) In* emission at 423 K (no probe laser was employed), 1 µs delay, and 100 µs gate width; (c) LIF at 423 K, 1 ms delay, and 8 µs gate width; (d) LIF at 883 K, 1 ms delay, and 8 µs gate width; (e) LIF at 883 K, 6 ms delay, and 100 µs gate width; (f) LIF at 883 K, 25 ms delay, and 500 µs gate width. The outlet of the reactor tube is indicated below (e), and the broken white line indicates the photolysis beam path. Generally, the images in each row are of interest to be compared. The LIF images represent vertical slices of the ground state indium distribution above the heater tube. Each image represents a different photodissociation event, at different points in time after the dissociation pulse. A video sequence depicting the spatially and temporally resolved planar LIF of several consecutive photodissociation events is provided in the supplementary material.

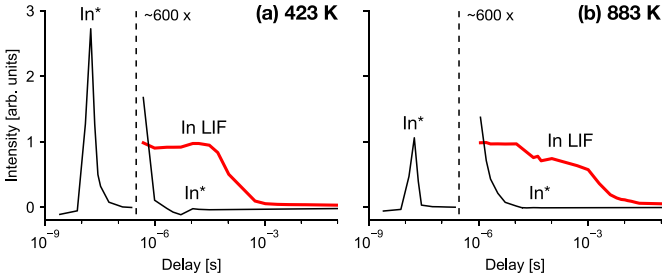

Figure 10. Time resolved In* emission and CW LIF, both collected at 451 nm, following 213 nm photolysis, at (a) 423 K, and (b) 883 K wall temperature. The solid black curve is the emission from indium produced in an excited state (In* emission) by the photodissociation of TMIn. The red curve is the indium LIF, representing the concentration of the ground state indium population. The indium LIF was collected at a higher camera intensifier gain compared to the In* emission. By comparison to the transient absorption measurements in figure 11(c), the LIF signal in the interval around 1 µs at 883 K corresponds to approximately 4 ppm indium concentration.

lower temperature, which can be understood as a smaller loss of TMIn to pyrolysis.

Shown in figure 11 are transient indium absorption signals following pulsed photolysis, for three different photodissociation pulse energies. Both the absorption and LIF signals represent the ground state population, but due to the smaller probe region (tighter focus) the absorption signal can be expected to decay faster than the LIF. At short delays (µs) a comparison can be made, however. In figure 11, the peak indium concentration produced directly after the photolysis is approximately 0.5, 2, and >4 ppm, at 5, 13, and 26 mJ cm^{-2} photodissociation laser fluence. Thus, the peak concentration in figure 11(c) corresponds to the LIF signal (red curves) in figure 10, which were collected under the same conditions.

The estimated concentration for indium generated by photodissociation of TMIn is far higher than the concentration of indium from pyrolysis only, which is in the order of a few ppb. Thus, heating during photolysis does not substantially contribute to the signal but acts to reduce the concentration of the TMIn precursor, and to extend the lifetime of the photolytically generated ground state atomic indium.

The peak In* emission intensity is associated with the peak indium concentration, determining the level of supersaturation, and the possibility of producing detectable indium particles. Its intensity at short delays is several orders of magnitude stronger than the LIF at microseconds or longer, but it should be emphasized that the In* emission and LIF signals are not directly comparable when it comes to quantitatively estimating the atomic indium concentration.

Finally, although the difference in diameter between the photolysis beam and the absorption beam relaxes requirements on precise alignment, a slight increase in sensitivity can be

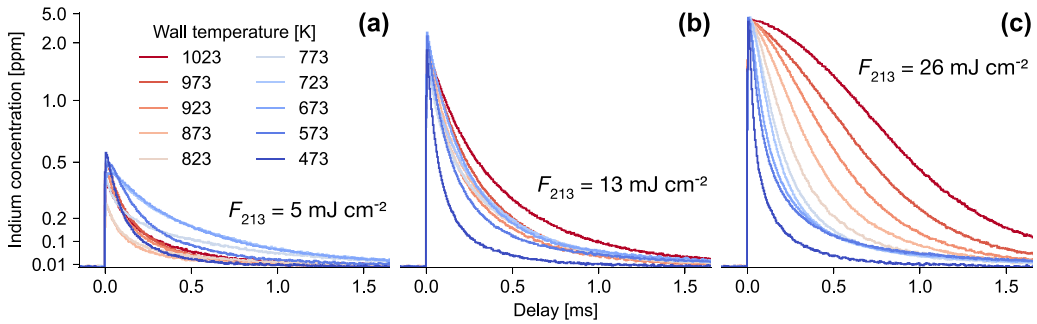

Figure 11. Transient single-pass absorption signal after photodissociation, at different temperatures, and photodissociation laser fluences F_{213}: (a) 5 mJ cm^{-2}, (b) 13 mJ cm^{-2}, (c) 26 mJ cm^{-2}. The different curves were collected at wall temperatures between 473 K (blue) and 1023 K (red). The probe wavelength was fixed at 410.2950 nm and each trace is an average of 40 photodissociation pulses.

expected if the angle between the photolysis beam and the absorption beam were reduced to approximately 10° or less.

4. Conclusions

In summary, optical measurements of pyrolysis and photolysis of TMIn vapor were demonstrated in chemical environments similar to epitaxy and aerotaxy nanowire growth conditions, providing spatially and temporally resolved absolute concentration of indium atoms released from dissociation of TMIn. Combining quantitative LIF measurements of species concentrations with gas phase temperature measurements using TLAF thermometry [15], will allow the spatial distribution of the two key parameters for aerotaxy nano-crystal growth to be non-intrusively monitored under operando conditions.

We have investigated the feasibility of controlling the dissociation of TMIn vapor in generating indium atoms photolytically using a pulsed laser at 213 nm. The generated atomic indium was detected using high-resolution laser spectroscopy; the concentration of indium atoms was measured using absorption spectroscopy and the spatial distribution was imaged using PLIF. Under typical aerotaxy operando conditions, the gas phase concentration of the pyrolytically generated atomic indium was determined to be in the order of few ppb, orders of magnitude higher than the equilibrium vapor concentration, whereas the photolytically generated indium reaches much higher concentration still. In vapor–liquid–solid growth of nanowires, concentration of the growth species (In) in the seed particles directly determines the supersaturation of the same [22], thus it can be expected that photolytic acceleration of the decomposition can have a corresponding influence on growth rate. The concentration of indium atoms generated by pulsed photolysis decayed within microseconds to a level of a few ppm, and the LIF signal was detectable even for delay times at tens of ms. Particles from homogeneous nucleation of indium was observed after the photodissociation using a 213 nm pulsed laser, suggesting the ability to optically manipulate the growth process.

Throughout this study, we have used TMIn as an example, however, similar approaches could be applied to other metalorganic precursors, e.g. TMGa and TMAl, commonly employed in epitaxial nanowire growth. UV photolytic control of the TMIn dissociation can potentially be used to enhance gold nanoparticle-seeded nanowire growth. At high temperature, parasitic reactions primarily at reactor walls becomes prevalent. UV photolytic growth of semiconductors allows growth at lower reactor temperatures resulting in improved material quality [23]. This can potentially be further aided by spatially confining precursor dissociation away from surfaces.

Finally, we have demonstrated how gated imaging of laser-generated particles can be immediately useful for non-intrusively determining flow patterns during the design of open-air aerotaxy reactors, without requiring introduction of intrusive tracer particles, or relying on computational fluid dynamics simulations.

Data availability statement

The data that support the findings of this study are available upon reasonable request from the authors.

Acknowledgment

This research was financially supported by the Knut and Alice Wallenberg Foundation.

ORCID iDs

Per Samuelsson https://orcid.org/0000-0003-0747-2150
Martin H Magnusson https://orcid.org/0000-0002-8049-2142
Knut Deppert https://orcid.org/0000-0002-0471-951X
Marcus Aldén https://orcid.org/0000-0003-3533-3588
Zhongshan Li https://orcid.org/0000-0002-0447-2748

References

[1] Hebner G A and Killeen K P 1990 Measurement of atomic indium during metalorganic chemical vapor deposition *J. Appl. Phys.* **37** 1598–600
[2] Woods V and Dietz N 2006 InN growth by high-pressures chemical vapor deposition: real-time optical growth characterization *Mater. Sci. Eng.* B **127** 239–50

[3] Huang Z S, Park C and Anderson T J 1993 Raman spectroscopic studies of gas phase Me_3In, Et_3In and $EtMe_2In$ *J. Organomet. Chem.* **449** 77–84
[4] Park C, Jung W-S, Huang Z and Anderson T J 2002 *In situ* Raman spectroscopic studies of trimethylindium pyrolysis in an OMVPE reactor *J. Mater. Chem.* **12** 356–60
[5] Hwang J Y, Park C, Jung J H and Anderson T J 2008 Homogeneous decomposition of trimethylindium in an inverted, stagnation-point flow reactor by *in situ* Raman spectroscopy *J. Electrochem. Soc.* **155** H124–9
[6] Richter W, Kurpas P, Lückerath R and Motzkus M 1991 Gas phase studies of MOVPE by optical methods *J. Cryst. Growth* **197** 13–25
[7] Heurlin M, Magnusson M H, Lindgren D, Ek M, Wallenberg L R, Deppert K and Samuelson L 2012 Continuous gas-phase synthesis of nanowires with tunable properties *Nature* **492** 90–95
[8] Sivakumar S, Persson A R, Metaferia W, Heurlin M, Wallenberg R, Samuelson L, Deppert K, Johansson J and Magnusson M H 2020 Aerotaxy: gas-phase epitaxy of quasi 1D nanostructures *Nanotechnology* **32** 025605
[9] Stringfellow G B 1999 *Organometallic Vapor-Phase Epitaxy* (San Diego: Academic) (https://doi.org/10.1016/B978-0-12-673842-1.X5000-5)
[10] Jacko M G and Price S J W 1964 The pyrolysis of trimethylindium *Can. J. Chem.* **42** 1198–205
[11] Larsen C A and Stringfellow G B 1986 Decomposition kinetics of OMVPE precursors *J. Cryst. Growth* **75** 247–54
[12] Beuermann T and Stuke M 1991 Photolysis of group III (Al, Ga, In) trimethyl compounds: detection of organic photofragments CH_3 and C_2H_6 by picosecond laser mass spectroscopy *Chem. Phys. Lett.* **170** 197–203
[13] Shenai-Khatkhate D V, DiCarlo R L Jr and Ware R A 2008 Accurate vapor pressure equation for trimethylindium in OMVPE *J. Cryst. Growth* **310** 2395–8
[14] Kaur D, de Souza A M, Wanna J, Hammad S A, Mercorelli L and Perry D S 1990 Multipass cell for molecular beam absorption spectroscopy *Appl. Opt.* **29** 119–24
[15] Hult J, Burns I S and Kaminski C F 2005 Two-line atomic fluorescence flame thermometry using diode lasers *Proc. Combust. Inst.* **30** 1535–43
[16] Deverall G V, Meissner K W and Zissis G J 1953 Hyperfine structures of the resonance lines of indium (In^{115}) *Phys. Rev.* **91** 297–9
[17] Alcock C B, Itkin V P and Horrigan M K 1984 Vapour pressure equations for the metallic elements: 298–2500 K *Can. Metall. Q.* **23** 309–13
[18] Shirai T, Reader J, Kramida A E and Sugar J 2020 NIST atomic spectra database (https://doi.org/10.18434/T4W30F)
[19] Koochesfahani M 1999 Molecular tagging velocimetry (MTV)—progress and applications *30th Fluid Dynamics Conf.* (*Norfolk, VA, US*) (https://doi.org/10.2514/6.1999-3786)
[20] Creighton J R, Coltrin M E and Fiegel J J 2008 Observations of gas-phase nanoparticles during InGaN metal-organic chemical vapor deposition *Appl. Phys. Lett.* **93** 171906
[21] Gurentsov E V 2017 UV laser synthesis of nanoparticles in the gas phase *Kinet. Catal.* **58** 233–54
[22] Wacaser B A, Dick K A, Johansson J, Borgström M T, Deppert K and Samuelson L 2009 Preferential interface nucleation: an expansion of the VLS growth mechanism for nanowires *Adv. Mater.* **21** 153–65
[23] Alberi K and Scarpulla M A 2018 Photoassisted physical vapor epitaxial growth of semiconductors: a review of light-induced modifications to growth processes *J. Phys. D: Appl. Phys.* **51** 023001